Journal of Sea Research 74 (2012) 2–7

Contents lists available at SciVerse ScienceDirect

Journal of Sea Research

journal homepage: www.elsevier.com/locate/seares

Absence of internal tidal beams due to non-uniform stratification

Theo Gerkema *, Hans van Haren

Royal NIOZ, P.O. Box 59, 1790 AB Den Burg, Texel, The Netherlands

ARTICLE INFO

Article history:
Received 5 August 2011
Received in revised form 21 March 2012
Accepted 21 March 2012
Available online 6 April 2012

Keywords:
Internal tides
Faeroe–Shetland Channel
Wave attractors

ABSTRACT

A linear internal-tide generation model is applied to the Faeroe–Shetland Channel, using observed profiles of stratification. Several degrees of simplification are considered: 1) uniform, i.e. constant N; 2) vertically varying N (z); 3) the full $N(x, z)$ and associated geostrophic background flows. It is shown that clearly identifiable internal tidal beams and internal-wave attractors occur in the first case, but not in the other cases where the pattern is patchy due to internal reflections from the strong inhomogeneities in the medium. Given the general occurrence of pycnoclines and geostrophic background flows in the ocean, it is argued that this internal scattering can be expected to be a widespread phenomenon.

1. Introduction

According to internal-wave theory, in a uniformly stratified fluid a superposition of modes amounts to the manifestation of beams, along which the energy propagates. Such a beam is expected to occur, for instance, over slopes where barotropic tides generate internal tides. Theory and numerical experiments have provided ample illustrations of this phenomenon, but oceanic observations tend to show little evidence of internal-wave beams. Only in rare cases does the data suggest the presence of a beam (and even then not unambiguously), e.g. in CTD profile yoyoing measurements (Pingree and New, 1991), in dissipation rates derived from microstructure data (Lien and Gregg, 2001; Lueck and Mudge, 1997), or in seismic images of fine structure (Holbrook et al., 2009).

Encouraging results were initially obtained in the Bay of Biscay in the 1990s when the internal tidal velocity field was measured using an ADCP, towed back and forth over a cross-slope distance of 15 km over the shelf break. These observations suggested the presence of an internal tidal beam descending into the deep ocean (Lam et al., 2004). However, later measurements, again in the Bay of Biscay but now over longer tracks stretching to 37 km off the shelf break, did not confirm this suggestion. The energy pattern turned out to be patchy over the larger scale; the connection with the theoretically predicted direction of energy propagation, as a coherent beam, was no longer evident (van Haren et al., 2010).

This patchiness has also implications for the occurrence of so-called internal-wave attractors. They may form in semi-enclosed basins due to multiple reflections of beams from the (sloping) side-walls, focussing the energy on a particular closed trajectory (Maas and Lam, 1995). Initially conceived in theory, they were soon demonstrated in laboratory experiments (Maas et al., 1997). It was speculated that they may occur in the ocean as well, and so, in the late 1990s, a project (called *PROcesses on the Continental Shelf*, PROCS) was set up by NIOZ to examine this through field measurements. The selected location was the Faeroe–Shetland Channel, whose geometry seemed a priori a favourable setting for the occurrence of internal-wave attractors. The logo of the campaign was suggestive of what was being sought (Fig. 1): in it, we see the basin's geometry (from above) superposed with, in a side view, the pattern of the wave attractor as observed in the laboratory by Maas et al. (1997).

In the event, no evidence was found of attractors nor even of distinct internal tidal beams (Hosegood et al., 2005). This lack of attractors was attributed to temporal and spatial variability of the buoyancy frequency (N) and background vorticity (Hosegood and van Haren, 2006). The present paper, by means of numerical modelling, demonstrates that spatial non-uniformities alone, in stratification, are already sufficient to break down internal tidal beams and attractors.

This work extends earlier results by Gerkema (2002), where the emphasis was on the baroclinic spring-neap cycle and spatial variations in the phase of that cycle. The buoyancy frequency was allowed to vary only vertically. Now, we take into account horizontal variations as well, which are very pronounced in the Faeroe–Shetland Channel. Instead of looking at spring-neap cycles, we consider here the pattern of the semidiurnal lunar internal tide (M_2) in isolation.

We briefly discuss observations from PROCS in Section 2. Then, in Section 3, equations are derived for linear internal-tide generation in the presence of non-uniform stratification and associated geostrophic flows. Model results are shown for situations of increasing complexity: from (i) uniform stratification (i.e., N constant) to (ii) a vertically varying N (z) to (iii) one with horizontal variations in N as well, along with geostrophic flows. The effect of these added features to the occurrence of internal tidal beams and attractors is discussed.

* Corresponding author.
E-mail address: gerk@nioz.nl (T. Gerkema).

1385-1101/$ – see front matter
doi:10.1016/j.seares.2012.03.008

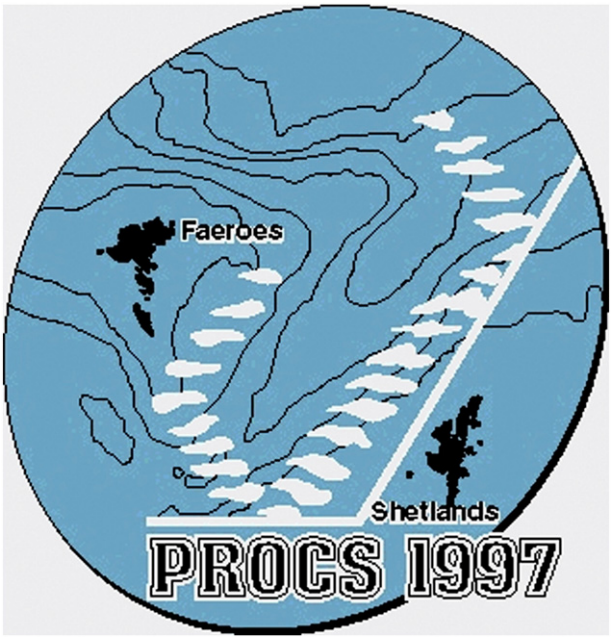

Fig. 1. Logo of the NIOZ project *PROCS*, projecting a side view of an internal-wave attractor from laboratory experiments onto the bathymetry of the Faeroe–Shetland Channel.

2. The PROCS campaign

In the framework of PROCS, two campaigns were carried out in the Faeroe–Shetland Channel in 1999 (and an earlier test campaign in 1997, which is not considered here):

- PROCS99-1: 14 April–5 May (van Haren and van Raaphorst, 1999)
- PROCS99-2: 21 September–13 October (Ridderinkhof, 1999).

The cross-channel transect where, on both occasions, CTD casts were taken, is shown in Fig. 2.

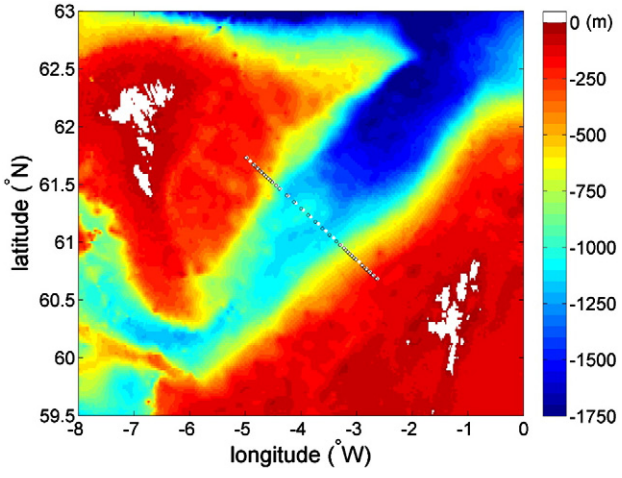

Fig. 2. Topography of the Faeroe–Shetland Channel, with depth in meters (based on Smith and Sandwell (1997)). A CTD section was made across the channel (black circles), on 27–29 April 1999; another one on 5–6 October 1999 along the same transect (white circles). In the upper left of this map lie the Faeroe Islands, in the lower right, the Shetland Islands. The Faeroe–Shetland Channel connects the Norwegian Sea in the north with the Faeroe-Bank Channel and the Wyville–Thompson Ridge in the south.

2.1. Hydrography of the Faeroe–Shetland Channel

The Faeroe–Shetland Channel forms an important pathway for the large-scale circulation (Fig. 3). At the Shetland (i.e., eastern) side of the channel, warm saline North-Atlantic Water flows northward into the Norwegian Sea, while Modified North Atlantic Water – a branch of the North-Atlantic Current – enters the channel from the north. Both are restricted to the upper 400 m. In the deeper layers, Arctic Intermediate Water flows southward along the Faeroe side of the channel, and still deeper (below 600 m), one finds the southward flowing Norwegian Sea Deep Water (Sherwin et al., 2008; Turrell et al., 1999). There is a lot of variability in these currents, though, partly due to eddies passing through the channel (Hosegood and van Haren, 2006; Sherwin et al., 2006).

The tilted boundaries between these water masses imply horizontal density gradients; they form an approximate geostrophic balance with the accompanying large-scale flows. Here, we will assume this balance to be exact, which allows us to deduce the vertical shear of the along-slope flow from the cross-slope CTD measurements.

2.2. Stratification

The temperature and salinity fields show a strong asymmetry in the cross-channel direction, which is reflected in the distribution of water masses (Fig. 3) as well as in the buoyancy frequency N.

Using the measured state variables temperature, salinity and pressure, we can calculate (in-situ) density ρ and the speed of sound c_s from the respective equations of state, which are based on the equation of state for the Gibbs potential (Feistel and Hagen, 1995). This equation of state has as the independent state variables temperature (T), salinity (S) and pressure (p), so the equation of state for density is of the type $\rho = \rho(T, S, p)$. This equation is applied locally, for every position. Since T and S depend both on the horizontal coordinate x and the vertical z, the resulting density field becomes a function of these spatial coordinates: $\rho(x, z)$. We can then define two different gradients, one with respect to x (leading to M^2, below), the other with respect to z features in the buoyancy frequency:

$$N^2 = -\frac{g}{\rho}\left(\frac{\partial \rho}{\partial z} + \frac{\rho g}{c_s^2}\right),$$

where g is gravity. (CTD measurements yield vertical profiles of temperature and salinity as function of pressure. The transformation of pressure to the vertical coordinate z was done using the expression proposed by Saunders (1981).)

The result is shown in Fig. 4 for both campaigns. In early spring only the deeper pycnocline is present, with a conspicuous asymmetry in the cross-channel direction. In early autumn, a shallower seasonal pycnocline is present as well.

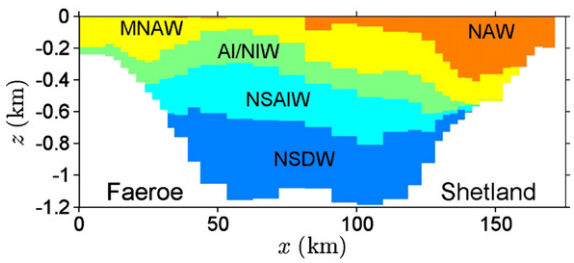

Fig. 3. Distribution of water masses defined in terms of ranges of potential temperature (following criteria in Turrell et al. (1999)) based on CTD data from PROCS99-1: North-Atlantic Water (NAW), Modified North-Atlantic Water (MNAW), Arctic Intermediate North Icelandic Water (AI/NIW), Norwegian Sea Arctic Intermediate Water (NSAIW), Norwegian Sea Deep Water (NSDW).

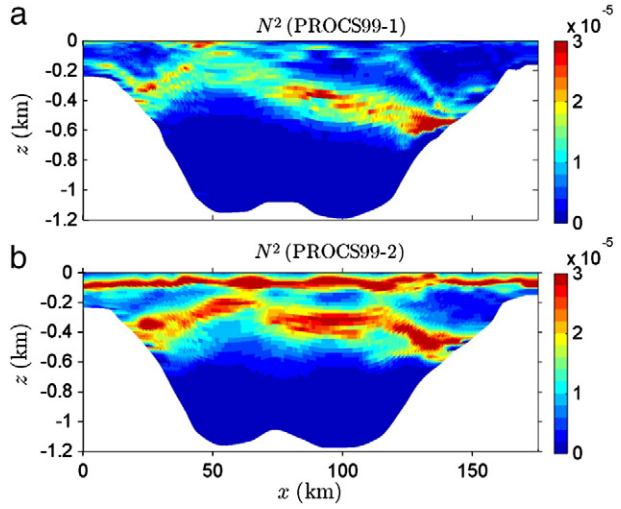

Fig. 4. Smoothed $N^2(x, z)$, in rad$^2 s^{-2}$, derived from CTD sections in a) early spring: 27–29 April 1999; b) early autumn: 5–6 October 1999. Smoothing was applied with an exponential moving average.

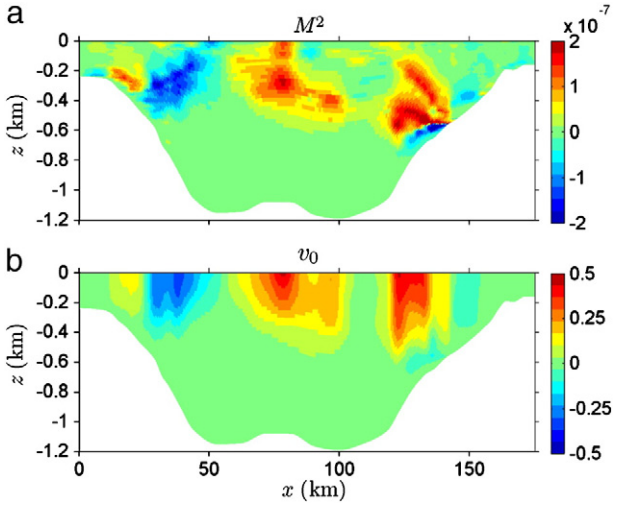

Fig. 5. Calculations based on the CTD profiles from PROCS99-1: in a) horizontal stratification M^2 in rad $^2s^{-2}$; b) the along-channel geostrophic flow v_0 in m s^{-1}, which is derived from M^2 assuming a level of no motion at the bottom. Positive flow means northeastward along the channel.

2.3. Geostrophic flows

For the numerical model, we need also, as background fields, the horizontal density gradients and associated geostrophic flows, which feature in the model equations (see below).

Analogously to N^2, the cross-channel (horizontal) gradient in in-situ density can be expressed as

$$M^2 = -\frac{g}{\rho}\frac{\partial \rho}{\partial x},$$

where x is the distance in the cross-channel direction.

Assuming geostrophic equilibrium (thermal-wind balance), we deduce from M^2 the vertical shear of an along-channel flow v_0,

$$\frac{\partial v_0}{\partial z} = M^2/f,$$

where f is the Coriolis parameter $f = 2\Omega sin\phi$, with latitude ϕ and Ω the Earth's angular velocity.

Vertical integration of this expression yields v_0, save for a 'constant' of integration $\tilde{v}(x)$. Finally, we can calculate $\partial v_0/\partial x$ (again, subject to an arbitrary function of x).

The N^2 and M^2, calculated from the raw data, suffered from a lot of stripiness, and were smoothed by using an exponential moving average. From the M^2 thus obtained, we calculated v_0 as indicated; the result for PROCS99-1 is shown in Fig. 5. In the calculation of v_0, we assumed that the flow vanishes at the topography; this fixes the aforementioned constant of integration. In the absence of further information, this choice is as good as any; the known meso-scale variability precludes the alternative way of using data from other studies, carried out at some other moment. We notice that the currents in the upper 400 m qualitatively agree with the overall large-scale pattern, dominated by a northeastward flow on the Shetland side (NAW) and a weaker southwestward flow on the Faeroe side (MNAW).

The horizontal shear $\partial v_0/\partial x$ (not shown) also features in the model equations; it attains values as large as the magnitude of the Coriolis parameter f, and is therefore bound to be significant in Eq. (12), derived below.

3. Model

In the model set-up, we assume uniformity in the along-channel direction (cf. Fig. 2), and examine the propagation in the cross-channel direction, under the assumptions of linear and hydrostatic theory.

3.1. Model equations

The equations for the propagation of internal waves in a geostrophic shear flow were established in previous studies, see, e.g., Mooers (1975):

$$u_t - fv = -p_x \tag{1}$$

$$v_t + fu + uv_{0,x} + wv_{0,z} = 0 \tag{2}$$

$$p_z = b \tag{3}$$

$$u_x + w_z = 0 \tag{4}$$

$$b_t + uM^2 + wN^2 = 0. \tag{5}$$

In these equations subscripts denote partial derivatives. Here, along-channel uniformity is assumed (i.e. $\partial/\partial y = 0$), we also made the hydrostatic approximation. The variable p denotes the departure of pressure from its hydrostatic value, divided by a reference value of density (ρ_*); b denotes buoyancy: $-g\rho/\rho_*$.

In our case, the fields u, v, w, p and b refer not merely to internal waves, but represent the combination of barotropic and baroclinic tides. We proceed by splitting the two, imposing a prescribed barotropic field:

$$U = Q\frac{cos\omega t}{h(x)}, \quad W = zQ\frac{cos\omega t}{h(x)^2}h_x.$$

The expressions follow from the assumption of a horizontally uniform, time-oscillating tidal transport. Here $z = h(x)$ represents the cross-channel topography; Q is the amplitude of the cross-slope barotropic tidal flux, and ω is the tidal frequency. Correspondingly, there are barotropic fields $V_t = -fU$ and $-P_x = U_t - fV$.

Writing now $u = u' + U$, and similarly for the other velocities and pressure, we obtain the equations for baroclinic (primed) variables:

$$u'_t - fv' = -p'_x \tag{6}$$

$$v'_t + fu' + u'v_{0,x} + w'v_{0,z} = -Uv_{0,x} - Wv_{0,z} \tag{7}$$

$$p'_z = b \tag{8}$$

$$u'_x + w'_z = 0 \tag{9}$$

$$b_t + u'M^2 + w'N^2 = -UM^2 - WN^2. \tag{10}$$

Notice that the field b has not been split; it contains both the barotropically induced vertical displacement of the isopycnals and the baroclinic response thus generated.

We introduce the stream function ($u' = \psi_z$, $w' = -\psi_x$), which allows us to reduce the set to three equations:

$$\psi_{zzt} - fv_z + b_x = 0 \tag{11}$$

$$v_t + \left(f + v_{0,x}\right)\psi_z - v_{0,z}\psi_x = -Uv_{0,x} - Wv_{0,z} \tag{12}$$

$$b_t + M^2\psi_z - N^2\psi_x = -UM^2 - WN^2. \tag{13}$$

Note that we dropped the prime in v', for convenience. These equations are solved numerically, with the imposed barotropic tidal flow U and W acting as the forcing. Also prescribed are the background stratification and associated geostrophic flow (i.e., N^2, M^2, $v_{0,x}$ and $v_{0,z}$), derived from the observed density field. The latter fields vary over the seasons, as Fig. 4 shows (and even, to a lesser extent, at time scales of weeks, see Hosegood et al. (2005)), but we will consider them to be time-independent within each model run.

Notice that the presence of a geostrophic flow, in combination with barotropic tides, adds forcing terms to the right-hand sides.

3.2. Numerical scheme

We use a 3rd-order Adams–Bashforth scheme in time, with 800 time steps per tidal period. In the horizontal direction, we have a uniform grid with steps of 400 m; horizontal gradients are evaluated with a 4th-order 5-point centered difference scheme. In the vertical, a collocation method is used, with 60 Chebyshev polynomials. A fourth-order spatial filter is used to selectively dampen oscillations on the grid scale (see Durran (1999)). Sponge layers are added on the shelves to prevent waves from reaching (and from reflection at) the boundaries of the numerical domain. In the results shown hereafter, the sponge layers are not included in the figures. Calculation starts from baroclinic rest (i.e. $\psi = v = b = 0$); the total duration of the calculation is 40 tidal periods, with the semidiurnal lunar period (M_2, 12 h 25 min 14 s).

Spin-up time differs somewhat between different experiments, but typically the steepest increase of the signal occurs within the first 12 periods, after which the amplitude becomes fairly steady in time except for an amplitude modulation at a 'beat' of about 14 periods. The forcing itself contains only a single frequency (M_2) and the model is linear, so the beat must reflect the period of a relatively weak part of the signal that travels around in the channel.

4. Results

The model Eqs. (11)–(13) are solved for three different cases, with increasing complexity. For PROCS99-1, the results are collected in Fig. 6.

4.1. Calculation with uniform N

First, we take the overall mean value of N^2 from all the CTD casts and use this single value to define a spatially uniform stratification, i.e. constant N. This amounts to a very radical simplification of the real situation. As a consequence, there are now no (horizontal) variations, so all the geostrophic terms in Eqs. (12) and (13) disappear: $M^2 = 0$ and $v_0 = 0$.

The result is plotted in terms of baroclinic cross-slope tidal velocity u, decomposed into amplitude and phase (Fig. 6a,b). As expected, the signal consists of well-defined internal-tidal beams. In fact, the pattern is very close to a typical attractor in parabolic basins, symmetric on the central vertical, as found theoretically by Maas and Lam (1995). This means that after being reflected from one side of the channel, the energy returns to its original position, following a closed loop.

A pattern like this had been expected to be found in the PROCS campaigns, based not only on the theoretical results by Maas and Lam (1995) but also on the empirical confirmation in the laboratory of the occurrence of internal-wave attractors (Maas et al., 1997). The explanation for the absence of any attractor in the actual field campaign must lie in the strong departure from the idealized situation considered here.

4.2. Calculation with N(z)

We take a first step towards the complexity encountered in the field by now allowing N to vary with z. We use the profile from the deepest station and apply it to all horizontal positions. Because of horizontal uniformity, there are still no geostrophic background terms in the model equations ($M^2 = 0$, $v_0 = 0$). This situation was earlier considered by Gerkema (2002), but the focus was then on the baroclinic spring-neap cycle and spatial variations in the phase of that cycle. Here, we adopt only one frequency (M_2) and focus instead on the effect of vertically varying stratification.

Notice that at the deepest station in PROCS99-1, there is not only a permanent pycnocline around a depth of 400 m, but also a weaker and shallower one at 100 m (Fig. 4a). Of both, the effect is noticeable in Fig. 6c, where the amplitude shows a clear change in structure around these depths. Moreover, the change in orientation of the beams near the deepest pycnocline is in accordance with the dispersion of internal waves, which predicts that internal-wave energy propagates more horizontally for larger N (see the formula in the caption of Fig. 8).

There are no longer continuous beams from surface to bottom in Fig. 6c, in contrast to the case of uniform stratification (Fig. 6a,b). Despite the fact that beams are broken up near the pycnocline, the overall pattern is still simple, especially so in the phase diagram (Fig. 6d), which consists of a few separate islands of near-uniform phase, being indicative of a standing-wave.

4.3. Calculation with all geostrophic terms (PROCS99-1)

Now we include the full spatial variation of the stratification, $N(x, z)$, as well as the horizontal density gradients in M and the geostrophic flow v_0; so all the terms in Eqs. (11)–(13) come into play. Fig. 6e,f shows that there are now merely patches of internal-wave signal, no well-defined beams anymore.

We also examined whether it would suffice to take into account $N(x, z)$ in the model equations while ignoring all the terms with M and v_0 (not shown). Although this is strictly speaking not dynamically consistent, it would be simpler from a modelling perspective (just allow N to vary spatially). However, it turns out that the difference from Fig. 6e,f is noticeable, in other words, the effects seen there cannot be captured by just the $N(x, z)$ term but the other terms with M and v_0 are important as well.

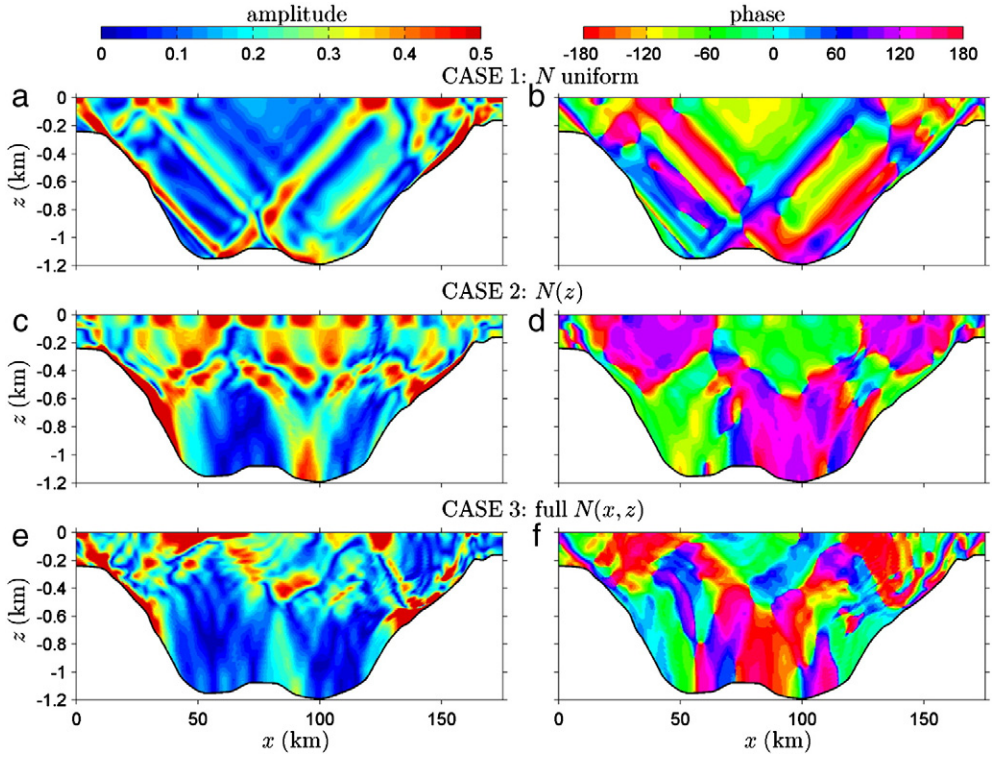

Fig. 6. Model results of internal tidal generation, showing the cross-slope baroclinic velocity component u, decomposed into amplitude in m s^{-1} (left panels) and phase in degrees (right panels). In a,b) stratification is taken uniform, i.e. N is constant (average over all CTD casts). In c,d) we have a horizontally uniform N, adopting the profile from the deepest station. In e,f) the full observed complexity of PROCS99-1 is taken into account: $N(x, z)$ along with M^2 and associated geostrophic along-channel flow v_0.

4.4. Calculation with all geostrophic terms (PROCS99-2)

For comparison with Fig. 6e, we also show the model results for the autumn data (PROCS99-2), which includes a seasonal pycnocline as well (Fig. 4b). Again, we take into account all the geostrophic terms. Fig. 7 shows that there are differences from the results for the spring situation, notably in the central upper part of the basin. Yet, one common feature is the strong current at the slopes, between depths of 400 and 600 m, which is in agreement with observations that also showed enhanced erosion and the formation of nepheloid layers in those bands, which were linked to enhanced measured M_2 internal tidal signals at those locations (van Raaphorst et al., 2001). Similarly, an abundance of mollusc fauna at mid-slope depths was found, related to enhanced resuspension (Witbaard et al., 2005).

5. Internal reflections

The explanation of the spatial incoherence seen in Fig. 6e,f lies in the occurrence of internal reflections due to the inhomogeneities of the medium, here featured by spatial variations in the buoyancy frequency N, horizontal density gradients and associated geostrophic shear currents. Repeated internal reflections deviate the energy from the original ray, thus causing blurred patterns of energy, as schematically depicted in Fig. 8. For these internal reflections to happen, variations of the medium should occur on spatial scales comparable to (or smaller than) the scale of the internal wave beams.

The dimensions of an unperturbed beam can be deduced from Fig. 6a, which shows a typical width of the order of 10 km, and a typical height of the order of 100 m. These are indeed the characteristic

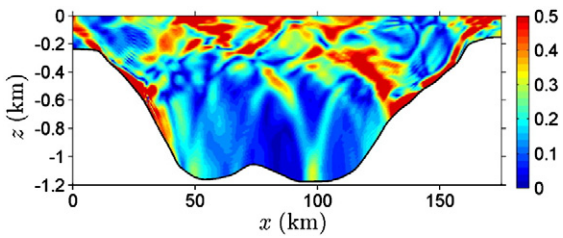

Fig. 7. Model result of internal tidal generation, showing the amplitude of the cross-slope baroclinic velocity component u in m s^{-1} for PROCS99-2. The full observed complexity is taken into account: $N(x, z)$ along with M^2 and accompanying geostrophic along-channel flow v_0.

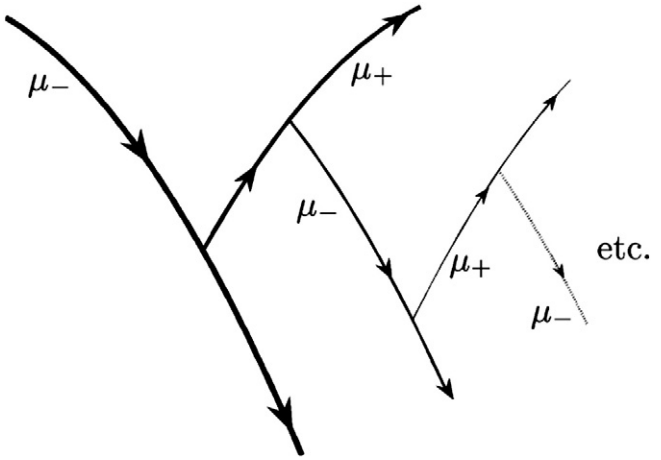

Fig. 8. An illustration of internal reflections due to a vertically varying N. The principal beam is on the left, arrows indicating down- and rightward energy propagation along a curve $\mu_- = \text{const}$. However, the inhomogeneities of the medium cause the energy to partially leave this path, diverting it to a path with up- and rightward propagation (μ_+). Similarly, energy partially leaves the latter path, continuing as down- and rightward propagation along a path $\mu_- = \text{const}$, etc. Here $\mu_\pm$ are defined by $dz/dx = \mu_\pm = \pm\{(\omega^2 - f^2)/(N^2(z) - \omega^2)\}^{1/2}$. Here a few discrete paths are sketched, as for internal reflections from an interface; in reality, this process is spatially continuous.

scales over which stratification and other background fields vary, see Figs. 4 and 5.

6. Conclusion

In this paper, we demonstrated that background variations in stratification, along with associated geostrophic flows, change the internal tidal field to such an extent that well-defined beams or internal-wave attractors are no longer present. This was shown using a linear internal-tide generation model. It may explain why beams and internal-wave attractors have been elusive in oceanic observations.

It is ironic that in the much simpler settings of laboratory experiments, internal-wave attractors can sometimes be hard to avoid even if the purpose is to study something else! A case in point is a series of experiments carried out on the Coriolis platform, Grenoble, in 2006. In a uniformly stratified channel (constant N), a slope was introduced at one end, while an oscillating piston at the other end created a barotropic tidal flow, generating internal tides over the slope. The original purpose of that study was to examine internal-wave reflection from the bottom and the generation of higher harmonics. Although these features were found, the signal turned out to be dominated by internal-wave attractors that quickly formed by reflections from the piston and the slope, back and forth, and so on.

So, while the setting is superficially similar to that of internal-tide generation in the ocean, like in Faeroe–Shetland Channel, the outcome was very different because the complexities of the oceanic stratification and associated geostrophic flows were not present in these laboratory experiments.

References

Durran, D.R., 1999. Numerical methods for wave equations in geophysical fluid dynamics. Springer. 465 pp.

Feistel, R., Hagen, E., 1995. On the GIBBS thermodynamic potential of seawater. Progress in Oceanography 36, 249–327.

Gerkema, T., 2002. Application of an internal tide generation model to baroclinic spring-neap cycles. Journal of Geophysical Research 107 (C9), 3124. doi:10.1029/2001JC001177.

Holbrook, W.S., Fer, I., Schmitt, R.W., 2009. Images of internal tides near the Norwegian continental slope. Geophysical Research Letters 36, L00D10. doi:10.1029/2009GL038909.

Hosegood, P., van Haren, H., 2006. Sub-inertial modulation of semi-diurnal currents over the continental slope in the Faeroe–Shetland Channel. Deep-Sea Research I 53, 627–655.

Hosegood, P., van Haren, H., Veth, C., 2005. Mixing within the interior of the Faeroe–Shetland Channel. Journal of Marine Research 63, 529–561.

Lam, F.P.A., Maas, L.R.M., Gerkema, T., 2004. Spatial structure of tidal and residual currents as observed over the shelf break in the Bay of Biscay. Deep Sea Research 51, 1075–1096.

Lien, R.C., Gregg, M.C., 2001. Observations of turbulence in a tidal beam and across a coastal ridge. Journal of Geophysical Research 106, 4575–4592.

Lueck, R.G., Mudge, T.D., 1997. Topographically induced mixing around a shallow seamount. Science 276, 1831–1833.

Maas, L.R.M., Lam, F.P., 1995. Geometric focussing of internal waves. Journal of Fluid Mechanics 300, 1–41.

Maas, L.R.M., Benielli, D., Sommeria, J., Lam, F.P., 1997. Observation of an internal wave attractor in a confined stably-stratified fluid. Nature 388, 557–561.

Mooers, C.N.K., 1975. Several effects of a baroclinic current on the cross-stream propagation of inertial-internal waves. Geophysical Fluid Dynamics 6, 245–275.

Pingree, R.D., New, A.L., 1991. Abyssal penetration and bottom reflection of internal tidal energy into the Bay of Biscay. Journal of Physical Oceanography 21, 28–39.

Ridderinkhof, R., 1999. Cruise report PROcesses on the Continental Slope. PROCS99-2, R.V. Pelagia cruise 64PE145, 21 September–13 October 1999, NIOZ.

Saunders, P.M., 1981. Practical conversion of pressure to depth. Journal of Physical Oceanography 11, 573–574.

Sherwin, T.J., Williams, M.O., Turrell, W.R., Hughes, S.L., Miller, P.I., 2006. A description and analysis of mesoscale variability in the Färoe–Shetland Channel. Journal of Geophysical Research 111, C03003. doi:10.1029/2005JC002867.

Sherwin, T.J., Hughes, S.L., Turrell, W.R., Hansen, B., Osterhus, S., 2008. Wind-driven monthly variations in transport and the flow field in the Faroe–Shetland Channel. Polar Research 27, 7–22.

Smith, W.H.F., Sandwell, D.T., 1997. Global sea floor topography from satellite altimetry and ship depth soundings. Science 277, 1956–1962.

Turrell, W.R., Slesser, G., Adams, R.D., Payne, R., Gillibrand, P.A., 1999. Decadal variability in the composition of Faroe Shetland Channel bottom water. Deep-Sea Research I 46, 1–25.

van Haren, H., van Raaphorst, W., 1999. Cruise report PROcesses on the Continental Slope. PROCS99-1, R.V. Pelagia cruise 64PE137, 14 April–5 May 1999, NIOZ.

van Haren, H., Maas, L.R.M., Gerkema, T., 2010. Patchiness in internal tidal beams. Journal of Marine Research 68, 237–257.

van Raaphorst, W., Malschaert, H., van Haren, H., Boer, W., Brummer, G.J., 2001. Cross-slope zonation of erosion and deposition in the Faeroe–Shetland Channel, North Atlantic Ocean. Deep-Sea Research I 48, 567–591.

Witbaard, R., Daan, R., Mulder, M., Lavaleye, M., 2005. The mollusc fauna along a depth transect in the Faroe Shetland Channel: is there a relationship with internal waves? Marine Biology Research 1, 186–201.